OPEN ACCESS
IOP Publishing | International Atomic Energy Agency
Nuclear Fusion
Nucl. Fusion **65** (2025) 066023 (16pp)
https://doi.org/10.1088/1741-4326/add484

Physics of beam-driven ion cyclotron emission in the large plasma device

O. Samant[1,*], R.O. Dendy[1], S.C. Chapman[1], S.K.P. Tripathi[2], T. Carter[2,3], B. Van Compernolle[2,4] and J.W.S. Cook[1,5]

[1] Centre for Fusion, Space and Astrophysics, University of Warwick, Coventry CV47AL, United Kingdom of Great Britain and Northern Ireland
[2] Department of Physics and Astronomy, University of California—Los Angeles, Los Angeles, CA 90095, United States of America
[3] Oak Ridge National Laboratory, Oak Ridge, TN 37830, United States of America
[4] General Atomics, San Diego, CA 92186, United States of America
[5] UKAEA (United Kingdom Atomic Energy Authority), Culham Campus, Abingdon, Oxfordshire OX14 3DB, United Kingdom of Great Britain and Northern Ireland

E-mail: Omstavan.Samant@warwick.ac.uk and omstavansamant@gmail.com

Received 15 November 2024, revised 11 April 2025
Accepted for publication 6 May 2025
Published 19 May 2025

Abstract

Ion cyclotron emission (ICE) is widely observed from spatially localised minority energetic ion populations in toroidal magnetically confined fusion (MCF) plasmas, both tokamaks and stellarators. Its spectral structure is typically regular with narrow suprathermal peaks, whose frequency separation matches a local energetic ion cyclotron frequency. Here we report the first computational (fully nonlinear self-consistent kinetic particle-in-cell code) and analytical (linear magnetoacoustic cyclotron instability (MCI)) studies of ICE observations from cylindrical plasmas contained in the Large Plasma Device (LAPD). Because LAPD is cylindrical, the plasma physics giving rise to the observed ICE spectrum necessarily excludes toroidal effects. Our approach, previously successful for toroidal plasma ICE, assumes slab geometry and hence is well adapted to LAPD. ICE from LAPD is strongly electrostatic, as distinct from electromagnetic, and is driven by 15 keV beam ions for which the ratio of perpendicular speed to the local Alfven speed, $v_\perp/v_A$, is 0.15, lower than in MCF plasmas from which beam-driven ICE has previously been observed. Our results are in good agreement with these observations. There is congruence between simulated ICE spectra, obtained in the saturated nonlinear regime of our computations, and observed ICE spectra; the underlying physics is essentially the same as in toroidal plasmas; and there is alignment with linear analytical theory where appropriate. The present work establishes a mapping from the cylindrical LAPD ICE observations to toroidal MCF ICE observations. The LAPD spectra are instances of beam-driven MCI-type ICE in its sub-Alfvenic, predominantly electrostatic manifestation, which has precedents in MCF stretching back to the 1990s. An interesting corollary is that, for many purposes, ICE in toroidal MCF plasmas 'might as well' be occurring in a cylinder.

* Author to whom any correspondence should be addressed.

Keywords: ion cyclotron emission, fast ions, energetic ions, LAPD, magnetoacoustic cyclotron instability, particle in cell (PIC)

(Some figures may appear in colour only in the online journal)

1. Introduction

The Large Plasma Device (LAPD)[1, 2] presents unique opportunities to investigate the effect of magnetic field geometry on the generation of ion cyclotron emission (ICE). Whereas ICE is widely observed from energetic ion populations in toroidal magnetically confined fusion (MCF) plasmas [3–47], both tokamaks and stellarators, in LAPD the confining magnetic field is cylindrical and the plasma more uniform. The LAPD plasmas whose ICE phenomenology is examined here are 19 m long and 60 cm in diameter. The majority thermal component of the plasma is composed of singly charged helium ions and there is a minority energetic spiralling beam of He^+ or H^+ ions injected into it. A variety of waves are spontaneously excited, spanning the shear Alfvén, ion cyclotron and lower hybrid frequency ranges [48, 49]. Here we focus on the ICE components. Its spectral structure is typically regular with sharp suprathermal peaks, whose frequency separation is identified with a local ion cyclotron frequency in the emitting region. ICE is typically excited in MCF plasmas under conditions where there is a spatially localised deviation of the minority energetic ions -for example, fusion born or beam-injected- from a Maxwellian velocity-space distribution [9, 10, 50]. This can result in their collective relaxation under the magnetoacoustic cyclotron instability (MCI), which is widely believed to underpin experimental observations of ICE.

The contemporary theory of the MCI has two strands. The linear analytical approach [9, 10, 50, 51] is based on calculations of combinations of kinetic dielectric tensor elements, summing over contributions from thermal ions and electrons together with the non-Maxwellian energetic ions. This essentially local, slab geometry, treatment has proven successful in capturing key features of the dependence of observed ICE spectra on local plasma conditions, and on the velocity-space distribution of the energetic ion population. Recently advanced by means of computational calculation of the kinetic dielectric integrals, linear MCI theory also explains aspects of the fine structure of observed ICE spectral peaks, including doublet splitting [52]. The second strand takes MCI theory into the fully nonlinear regime, by means of first principles gyro-resolved kinetic treatments embodied in particle-in-cell (PIC) [53, 54] codes. These self-consistently solve the Lorentz force law and Maxwell's equations for tens of millions of gyromotion-resolved energetic and thermal ions, together with electrons and all vector components of the electric and magnetic fields. Applied to the MCI, the PIC code EPOCH [55] yields simulated ICE spectra in the saturated regime, including their polarisation (in particular, electromagnetic versus electrostatic), for direct comparison with observed ICE spectra. These EPOCH PIC simulations of ICE achieve good agreement with observations [12, 15, 41, 42, 46, 47, 56, 57], including recently the variation of spectral structure with the isotopic mix of thermal ions [58], and are carried out in locally uniform slab geometry with fixed magnetic field strength and plasma number density. Importantly, the growth rate of particle and field energies inferred at early times from the PIC simulations can be shown to be that predicted by the analytical theory of the MCI for corresponding initial parameters [45].

Both strands of contemporary MCI theory are in locally uniform slab geometry, thus omitting the magnetic field gradients and curvature, together with density gradients, that are fundamental to toroidal MCF plasmas. The success of MCI theory in nevertheless matching observed ICE spectra is taken to indicate that the plasma physics of ICE is strongly localised, with localisation determined by the small spatial region in which substantial deviation from the Maxwellian arises in the velocity-space distribution of the minority energetic ion population which drives ICE. This localisation is also responsible for the narrowness of ICE spectral peaks, with the local cyclotron frequency in the emitting region correspondingly well defined. In the case of ICE driven by 3.5 MeV fusion-born alpha-particles in deuterium-tritium plasmas, or by 3 MeV fusion-born protons in pure deuterium plasmas, it has been shown that this localisation can arise from drift orbit effects [12]. ICE driven by neutral beam injected (NBI) ions usually arises from a location in the plasma near the injection point at the edge, where the velocity-space distribution of freshly ionised particles approximates a delta-function [12, 15, 41, 42]. ICE from the core plasma, sometimes transient, is also increasingly found, see for example [14–16, 21–24, 43].

Given the widespread current use of ICE as a diagnostic for energetic ion populations in toroidal MCF plasmas, together with its potential in relation to fusion-born ions in future aneutronic plasmas where neutron-based diagnostics will be inapplicable, it is important to test the model assumptions and observational inferences wherever possible. Observations of ICE from the cylindrical LAPD plasma provide a fresh perspective with respect to the success of the slab geometry approximation when modelling ICE, and, as we discuss below, with respect to other aspects of ICE phenomenology. These aspects include: the polarisation of ICE signals—in particular, electromagnetic vs electrostatic—which is important for their detection and measurement; how the polarisation of ICE depends on the ratio of the energetic ion velocity (perpendicular, $v_\perp$, and parallel, $v_\parallel$, to the local magnetic field direction) to the local Alfvén speed v_A; the consequences for the spectral structure of ICE spectrum of the substantial velocity component $v_\parallel$ possessed by beam ions in LAPD; and the ways in which

the lower hybrid frequency ω_{LH}, above which the fast Alfvén wave is evanescent, affects the envelope of the ICE spectrum, see for example [11].

The ICE from LAPD considered here is driven by injected beam ions for which $v_\perp/v_A = 0.15$, a value lower than in MCF plasmas from which NBI-driven ICE is typically observed. This ICE signal is strongly electrostatic, as distinct from electromagnetic. Electrostatic NBI-driven ICE spectra were observed from deuterium–tritium (DT) supershot plasmas in the Tokamak Fusion Test Reactor (TFTR), see for example figures 1 and 2 of [10], and interpreted theoretically there in terms of an electrostatic limit of the linear analytical MCI. Beam-driven ICE was previously detected from smaller tokamak plasmas like the Princeton Divertor Experiment [59], together with smaller-scale experiments [60, 61]. The observations of electromagnetic ICE from super-Alfvénic fusion-born alpha-particles in DT plasmas in the Joint European Torus (JET) underlined the importance of understanding the relationship between ICE driven by beam ions and ICE driven by fusion-born ions, a synthesis for which was provided in [7]. There, ICE spectral peaks at harmonics of the alpha-particle cyclotron frequency, evaluated at the outer midplane plasma edge, were observed at the onset of the beam injection phase of TFTR supershots and persisted for approximately 100 ms–250 ms. This was in contrast with observations of ICE from JET, where alpha-particle cyclotron harmonic peak intensities evolved with the density of alpha-particles at the plasma edge. These differences were found to be due to the fact that newly-born fusion alpha-particles were super-Alfvénic near the edge of JET plasmas, but sub-Alfvénic near the edge of TFTR supershot plasmas, see for example figure 6 of [7]. In TFTR plasmas with edge densities such that newly-born alpha-particles were super-Alfvénic, alpha-particle cyclotron harmonic ICE spectral peaks were observed to persist. These results were in qualitative agreement with analytical linear growth rates of the MCI in the differing plasma regimes; see also the analysis for sub-Alfvénic alpha-particles under TFTR conditions in [62], where characteristic values of $v_\perp/v_A$ are in the range 0.3–0.5.

More recently, studies of the dependence of observed ICE spectra on the value of $v_\perp/v_A$ for the driving beam ions have been carried out on the LHD heliotron-stellarator [41, 42]. This work has benefited from the application of fully nonlinear PIC simulations, which were not available at the time of the TFTR and JET DT ICE studies. In [41], the transition in ICE phenomenology across the boundary $v_\perp/v_A = 1$ was addressed. The variation of ICE spectral structure with edge plasma density, spanning values of $v_\perp/v_A$ between 0.6 and 0.36 for the NBI ions, was found to be well matched by PIC MCI simulations in [42]. These results partly motivated predictive studies for future ICE measurements in the W7-X stellarator [63], for which $v_\perp/v_A = 0.14$, comparable to the LAPD regime considered here. The polarisation of the predicted ICE spectrum in W7-X was found to be predominantly electrostatic, except at the lowest cyclotron harmonic peaks. Electrostatic aspects of the MCI are also of interest because of potential interplay with the lower hybrid drift instability at high cyclotron harmonics as considered in [64, 65], for example.

Finally, we note that the beam ion injection angle in LAPD is such that the value of $v_\parallel/v_A$ can be substantial. This creates a potential link to recent observations of ICE from fusion-born protons in deuterium plasmas in LHD [43], where frequency shifts arising from high $v_\parallel$ are central to the observed ICE phenomenology, see e.g. figure 2 of [43], and to its PIC-based interpretation in terms of the MCI, see e.g. figure 16 of [43].

In summary, there are multiple points of contact between LAPD ICE observations, together with the new PIC-based modelling and interpretation results presented in this paper, and contemporary frontier aspects of ICE from toroidal MCF plasmas.

2. Observed ICE spectra from LAPD

We refer to [48, 49] for a systematic account of the LAPD plasma configuration and detection equipment used to obtain the ICE spectra shown in figure 1. Figure 1 shows two power spectra of the electric field component E_x observed from Helium plasmas with 15 keV He^+ beam in LAPD using a dipole probe. Each of the panels shows the 'beam on' and 'beam off' spectra: only with the beams present is there excitation of ICE. Some of the key features observed are an extensive set of sequential ion cyclotron harmonic spectral peaks, ranging from around 10 $\omega_{c\mathrm{He}^+}$ to around 70 $\omega_{c\mathrm{He}^+}$ fading out close to the lower hybrid frequency $\omega_{\mathrm{LH}} \sim 77\omega_{c\mathrm{He}}$, visible in the electric field; and a broad overall structure, peaking around the 35th harmonic. We note that the electronics and the probe used for these measurements were maximally sensitive in the range of about $10\omega_{c\mathrm{He}^+}$ to $350\omega_{c\mathrm{He}^+}$[49], hence any ICE at lower harmonics may not have been detectable. We aim to study the physics which gives rise to these distinctive features of LAPD ICE, which are reproducibly observed in other similar LAPD plasmas.

3. Simulation of ICE from LAPD

We use the EPOCH PIC code [55] to simulate the plasma scenarios relevant to LAPD. We adopt a 1D3V simulation domain which comprises a one dimensional spatial domain oriented at a chosen angle to the ambient magnetic field, while including all three dimensions in velocity space, thus capturing ion and electron gyromotion. This approach, while requiring significant but feasible amounts of computational resources, has been successfully employed previously to model MCI physics for simulation and interpretation of ICE observations from beam heated plasmas in the KSTAR [12] and D-IIID [15] tokamaks and the LHD heliotron-stellarator [41, 42] for example. EPOCH self consistently evolves the electric and magnetic fields in space and time, defined on a Yee staggered grid, using Maxwell's equations with a finite-difference time-domain method alongside the gyro-orbit resolved charged particle

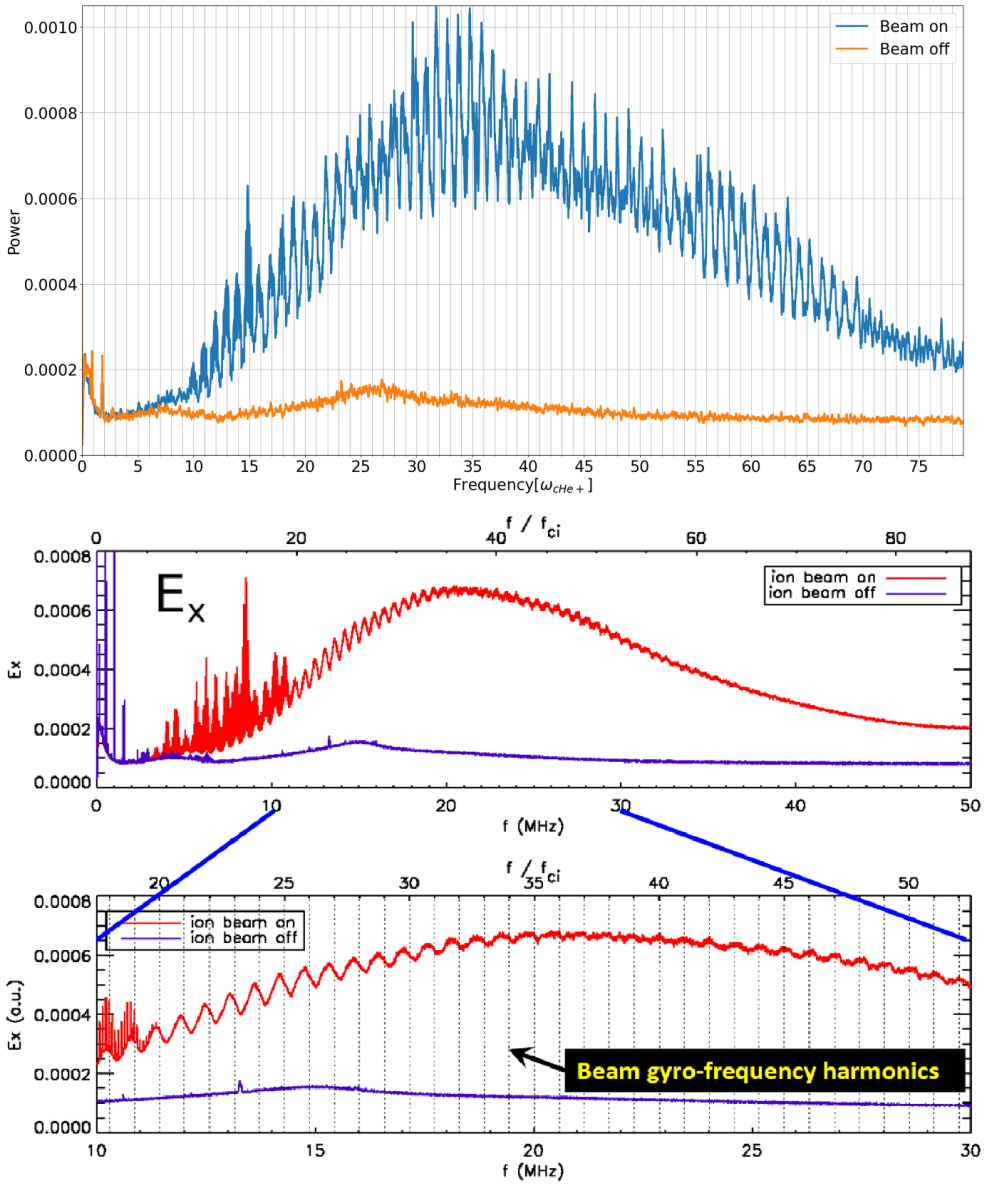

Figure 1. Two experimentally observed power spectra of the electric field, observed using a dipole probe in a Helium plasma with a 15 keV He+ beam in LAPD. The y-axis denotes the intensity in arbitrary units and the x-axis corresponds to the frequency in units of ion cyclotron frequency and MHz. A distinctive feature of these ICE spectra is that ion cyclotron harmonic peaks are observed up to very high harmonics fading out close to the lower hybrid frequency, $\omega_{\mathrm{LH}} \sim 77\omega_{c\mathrm{He}}$ in these cases. There is also an overall broader peak around the 35th harmonic, with finer cyclotron harmonic peaks visible overlapping it. The spectrum on the bottom is reproduced with permission from [49].

dynamics using a modified Boris algorithm. The charged particles obey the Lorentz force law under the instantaneous local electric and magnetic fields and are represented by macroparticles weighted on the grid using a fifth-order scheme to reduce noise. The electron and thermal ion (singly charged Helium) populations are initialised as a pseudorandom Maxwell distributed thermal background. The minority energetic beam ions (He^+ or H^+) are initialised with a ring-beam distribution given by

$$f(v_{\parallel}, v_{\perp}) \propto \exp\left(-\frac{(v_{\parallel} - v_d)^2}{v_r^2}\right) \exp\left(-\frac{(v_{\perp} - u_0)^2}{u_r^2}\right). \quad (1)$$

Table 1. Physical parameters used in the EPOCH PIC simulations of ICE from LAPD.

Parameter	Value (He^+ beam cases)	Value (H^+ beam cases)
Electron density (n_e)	$1.5 - 3.0 \times 10^{16}$ m^{-3}	2.3×10^{17} m^{-3}
Thermal e^- and He^+ temperature	7 eV	7 eV
Magnetic field	0.15T	0.18 T
Beam injected ion energy	15 keV	15 keV
Beam ion density	$0.0233 \times n_e$	$0.0304 \times n_e$
Beam pitch angle	35°	53°
Initial drift along B (v_d)	6.94×10^5 m s^{-1}	1.02×10^6 m s^{-1}
Initial perpendicular velocity (u_0)	4.86×10^5 m s^{-1}	1.35×10^6 m s^{-1}
Perpendicular velocity spread (u_r)	$0.001 \times u_0$	$0.001 \times u_0$
Parallel velocity spread (v_r)	$0.1 \times v_d$	$0.1 \times v_d$

Here $v_\perp$ and $v_\parallel$ are the velocity components perpendicular and parallel to the background magnetic field; u_0 is the initial perpendicular velocity and v_d is the initial bulk velocity along the background magnetic field, whose values are determined by the energy of the injected beam and its orientation with respect to the magnetic field; and u_r and v_r are the perpendicular and parallel velocity spreads respectively. In its zero-thickness limiting case of a product of drifting delta-functions, motivated by drift orbit studies(see figure 14 of [4], figure 2 of [7], figure 2 of [13] and table 1 of [43]), equation (1) has been used successfully in modelling ICE from fusion-born ion populations in JET [50], TFTR [62], KSTAR [13] and LHD [41]. Inclusion of limited thermal spread has been studied in [52, 56, 66]. In the present study, the system of thermal electrons and ions with the energetic ion ring-beam, once initialised, is then allowed to evolve self-consistently over several ion gyroperiods.

The CFL (Courant–Friedrichs–Lewy) condition [67] for the time step is satisfied to within a factor of 0.95. A standard requirement of PIC simulations is to resolve the electron Debye length λ_{D_e} to capture the associated plasma physics. Furthermore, in order to prevent numerical heating of the species with the smallest gyroradius (in this case, the electrons), the grid cells must be sufficiently small to resolve the corresponding (electron) gyroradius. The cell size used in our simulations varies from $0.36\lambda_{D_e}$ to $0.83\lambda_{D_e}$ depending on these parameters with the spatial domain along x and the externally applied magnetic field in the xz plane. The simulation spatial domain must be long enough to encompass several gyroradii of the beam ions. Taken together, these constraints require us to use 200 000 cells for each simulation. In addition to these requirements on the spatial resolution, we must also satisfy the Nyquist condition in the wavenumber space such that dk, the resolution in wavenumber space, is smaller than ω_c/v_A, where ω_c is the ion cyclotron frequency and v_A is the Alfvén velocity. Given that characteristic frequencies are of the order of the ion cyclotron frequency and its harmonics, and that the MCI is a cyclotron resonant wave-particle phenomenon, ω_c must be resolved by the angular frequency resolution $d\omega$, meaning the simulation must run for several gyroperiods. We run the simulations for $12\tau_{gHe+}$ in the H^+ beam cases and $8\tau_{gHe+}$ in the case of He^+ beam. The Nyquist frequency, which is dependent on the sampling rate, should be large enough to reduce aliasing from affecting the region of interest. Due to memory limitations, the simulation data cannot be saved at every timestep. However, it must still be stored at sufficient cadence to accurately capture the physics being investigated. Finally, since noise is inversely dependent on the square root of the number of macroparticles, we use 100 particles per cell for each species.

3.1. Modelling the observed LAPD ICE spectra

Using the computational approach described above, we run simulations of He^+ plasma with a minority energetic ion beam population, either He^+ or H^+. The parameter set for the He+ beam is chosen to match the LAPD conditions which gave rise to the observed ICE spectrum shown in figure 1, whereas the H+ beam case is a theoretical study intended to explore adjacent parametric dependencies in regimes that might give rise to ICE spectra similar to figure 1. The relevant parameters are given in table 1. The simulation domain is oriented obliquely at 89.5° with respect to the direction of the magnetic field following from the theory discussed in [50] as well as to allow for the observation of parallel propagation effects. The He beam pitch angle is based on the computed ion beam trajectory from the injection angle. The ion temperatures were not measured in the specific experiments with ICE observations but have been measured in comparable experiments to be in the order of 1 eV. In the absence of direct measurements of plasma temperature, we estimated values using IAEA Helium charge state estimates using FLYCHK [68], to match the highly ionised thermal species assumed in the simulation. However, the thermal ions do not play a major role in the stability of MCI because the thermal ions get Doppler-shifted out of cyclotron resonance with the beam-excited harmonics. They just provide an invariant inertial load supporting the excited waves, which is independent of temperature. MCI entails a collective relaxation of the non-Maxwellian fast ion population, specifically the beam ions in our simulations as seen in figure A4. The time traces in figure 2 follow this collective relaxation through the loss of energy from the fast ions, transferred to the thermal ions and electrons and to the electric and magnetic fields. The excited fields are predominantly electrostatic rather than electromagnetic as quantified by the traces for the electric field E_x and

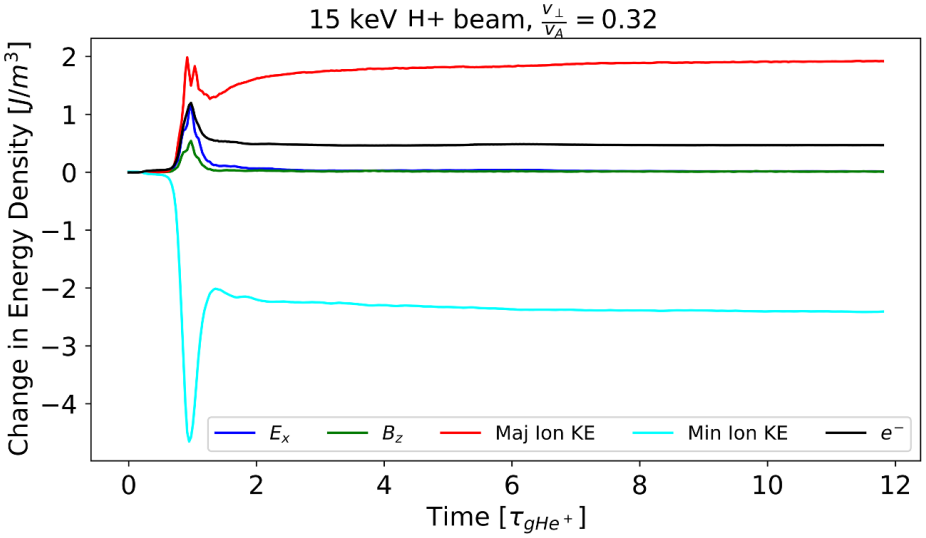

Figure 2. Time evolution of particle and field energy densities for the He^+ plasma with 15 keV H^+ beam case(2nd parameter set in table 1). The minority beam ions lose energy which is gained by the thermal ions and electrons together with the spontaneously excited via the electric and magnetic fields. The energy acquired by the electrostatic field component E_x is dominant compared to that in the electromagnetic component B_z.

magnetic field B_z in figure 2. This is consistent with the observations of predominantly electrostatic ICE shown in figure 1 and motivates the deeper study of the electric field E_x output data which follows.

In order to identify the mode structure of the excited fields, E_x is first stacked in a 2D matrix with time evolution along one axis and spatial location in the other. Taking a 2D FFT then provides us with the spatiotemporal Fourier transform of the E_x data, resolving it into its different wavenumber and frequency components. Figure 3 shows the 2D spatiotemporal FFT of the electric field E_x data from our simulation of an H^+ beam in an He^+ plasma, for the parameters given in the rightmost column of table 1. The parabolic feature extending diagonally upwards from the origin can be matched with the cold plasma dispersion relation of the fast Alfvén wave (equation (5.49) in [69]). The horizontal lines correspond to ion cyclotron harmonics. At the intersection of these two features, the degeneracy between the fast Alfvén wave and the ion cyclotron harmonic—ion Bernstein branch is resolved clearly in this high resolution simulation. We see harmonics extending past the flattening of the fast Alfvén wave and a strong extended feature, both around $15\omega_c$. These harmonics can be seen as spectral peaks in the associated stimulated ICE power spectrum, figure 6, discussed below.

Figure 4 shows the 2D spatiotemporal FFT of the E_x data from the He^+ plasma with He^+ beam. This shares several features with the experimental spectra shown in figure 1. There is a succession of cyclotron harmonic peaks which continue far into the frequency space, together with an extended structure around the flattening of the Fast Alfvén wave. The intensity of this extended feature exceeds that of the ion cyclotron harmonic features in both figures 3 and 4. We also note that in figure 4, the harmonics split and rejoin around the frequency $35\omega_c$ and wavenumber 600 $\frac{\omega_c}{v_A}$. This is discussed further below.

The features of the observed ICE power spectra of the electric field, distinctive to the LAPD plasmas, shown in figure 1, can be compared with those of our simulated power spectra. These are obtained from the E_x field properties captured in figures 3 and 4 by integrating the power at each discrete frequency interval over wavenumber space. Figure 5 shows E_x power spectra for two PIC simulations with different plasma densities, for the 15 keV He^+ beam. Figure 6 shows a PIC simulation E_x power spectrum for a 15 keV H^+ beam case. In both figures there are sequential harmonic peaks extending up to high cyclotron harmonics fading out close to the corresponding lower hybrid frequencies, $\sim 40\omega_{c\mathrm{He}^+}$ and $\sim 50\omega_{c\mathrm{He}^+}$ for figure 5, and $\sim 29\omega_{c\mathrm{He}^+}$ for figure 6. These harmonics are predominantly electrostatic in both experiment and simulation. Above the lower hybrid frequency, we expect a region of evanescence (see e.g. appendix A of [11]), and also note that it is possible for nonlinear MCI drive to excite cyclotron harmonic features in this region, both experimentally(figures 1 and 3 of [11]) and in corresponding simulations(figures 4 of [11]). A broader peak is observed, around 25 $\omega_{c\mathrm{He}^+}$ and 35 $\omega_{c\mathrm{He}^+}$ for figure 5 and 16 ω_c for figure 6, close to the flattening of the fast Alfvén wave similar to that observed in figure 2 of [63] which also addresses a predominantly electrostatic ICE scenario.

3.2. *Comparison of nonlinear simulation results with linear theory*

In figure 4, the cold plasma dispersion relation for the fast Alfvén wave (equation (5.49) in [69]) intersects the diagonal

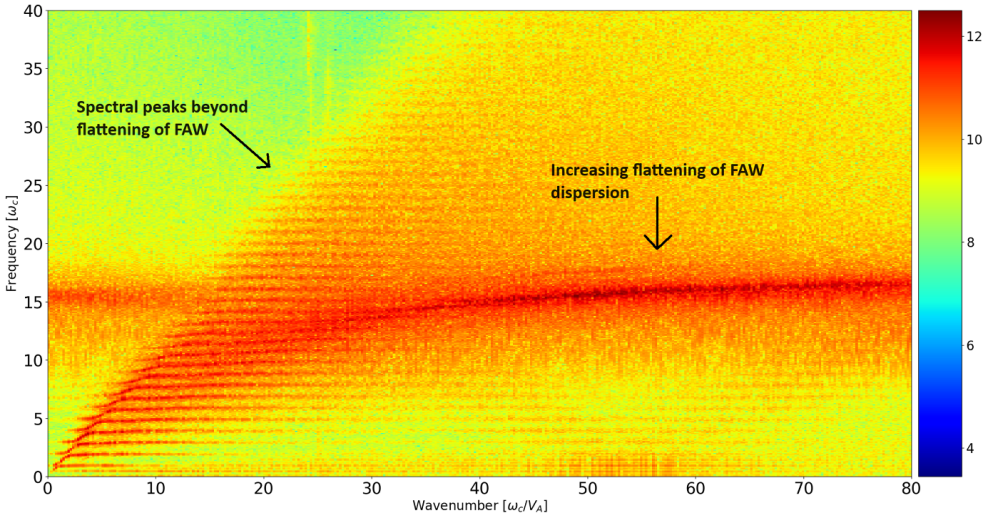

Figure 3. Spatiotemporal Fourier transform of the E_x field component generated in our PIC simulation of the relaxation of a 15 keV H^+ beam in an He^+ LAPD plasma for the second parameter set in table 1, showing the fast Alfvén wave along with excited ion cyclotron harmonics. The logarithmic (base ten) colour scale quantifies the relative distribution of energy across frequency-wavenumber space. Frequency is normalised to the proton cyclotron frequency ω_{cp} and wavenumber to the ratio of ω_{cp} to Alfvén velocity v_A. The simulation resolves the degeneracy at the intersections between the dominant normal modes, which arise spontaneously in the simulation. These are the fast Alfvén wave, on the diagonal at low frequencies $\leqslant 10\omega_{cp}$, then flattening towards the horizontal axis at frequencies approaching $15\omega_{cp}$; and sequential quasi-horizontal branches of the ion cyclotron harmonic—ion Bernstein branch wave. The corresponding distributions of excited field energy with respect to the frequency(the power spectrum) shown in figure 6 are obtained by integrating this plot over all wavenumbers.

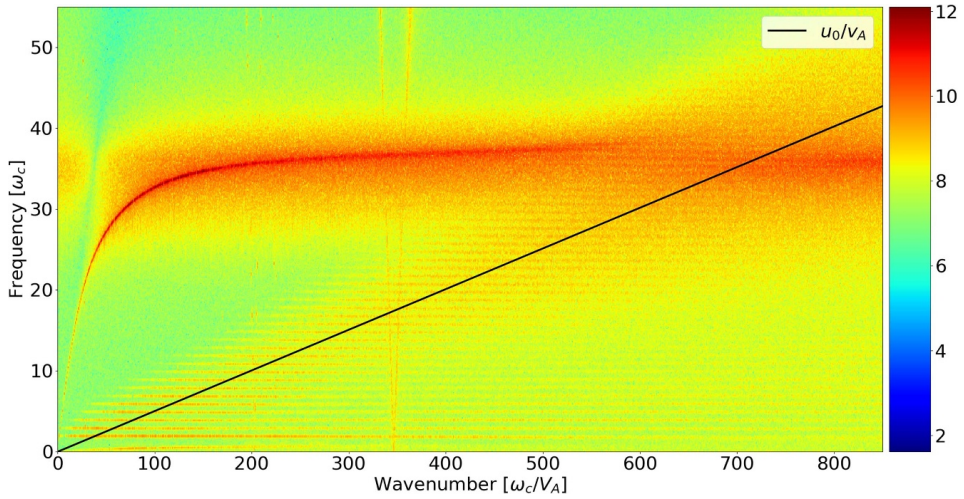

Figure 4. Spatiotemporal Fourier transform of the E_x field component generated in our PIC simulation of the relaxation of a 15 keV He^+ beam in an He^+ LAPD plasma for the first parameter set ($n_e = 3.0 \times 10^{16}$ m^{-3}) in table 1 showing the fast Alfvén wave along with excited ion cyclotron harmonics. The logarithmic (base ten) colour scale quantifies the relative distribution of energy across frequency-wavenumber space. Frequency is normalised to the singly ionised Helium cyclotron frequency $\omega_{c\mathrm{He}^+}$ and wavenumber to the ratio of $\omega_{c\mathrm{He}^+}$ to Alfvén velocity v_A. The black diagonal line shows where the phase velocity matches the initial perpendicular speed of the beam ions: $\frac{\omega}{k} = u_0$ as defined by equation (1) and normalised to v_A. It is evident that this condition strongly influences the location of field excitation in (ω, k) space.

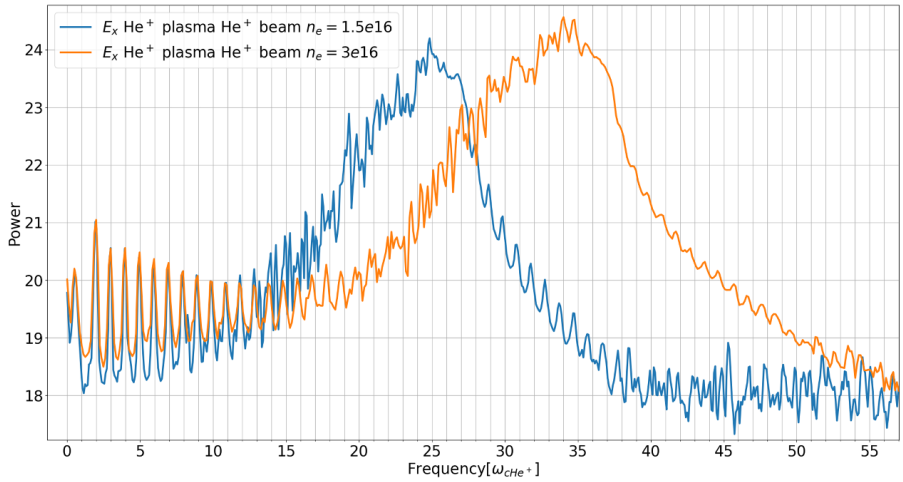

Figure 5. Two simulated electrostatic E_x ICE power spectra, for 15 keV He$^+$ beam injection into He$^+$ LAPD plasma, for electron number densities $n_e = 1.5 \times 10^{16}$ m^{-3}(blue) and 3.0×10^{16}(orange). These power spectra are obtained by integrating spatiotemporal Fourier transforms such as figure 4 over wavenumber. They are qualitatively similar to the experimental spectra shown in figure 1(upper), including the electrostatic ICE harmonic spectral peaks extending far past the broad peak around $25\omega_{c\mathrm{He}^+}$(blue) and $35\omega_{c\mathrm{He}^+}$(orange) and fading out close to the lower hybrid frequencies, $\omega_{\mathrm{LH}} \sim 40\omega_{c\mathrm{He}^+}$ and $\omega_{\mathrm{LH}} \sim 50\omega_{c\mathrm{He}^+}$ respectively.

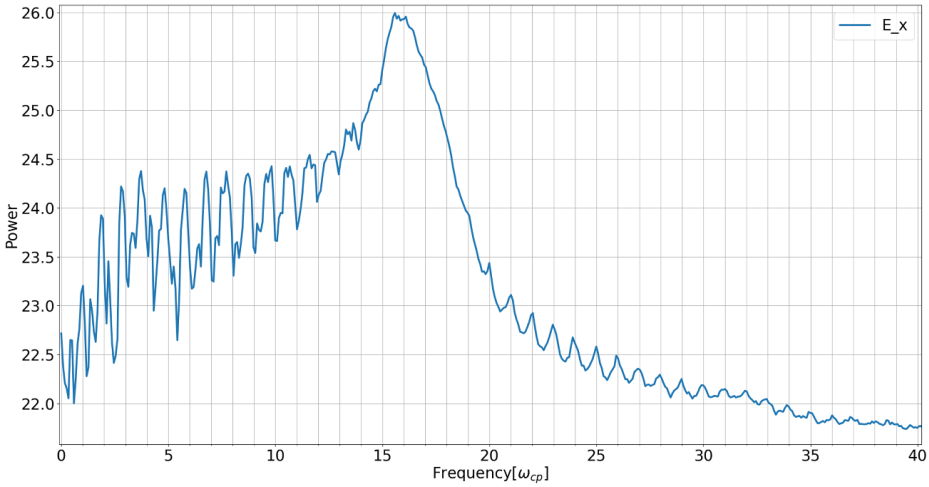

Figure 6. Simulated electrostatic E_x ICE power spectrum, for 15 keV H$^+$ beam injection into He$^+$ LAPD plasma, for electron number density $n_e = 2.3 \times 10^{17}$(blue). This power spectrum is obtained by integrating the spatiotemporal Fourier transform shown in figure 3 over wavenumber. It is qualitatively similar to the experimental spectra shown in figure 1, including the electrostatic ICE harmonics spectral peaks extending far past the broad peak.

line where the phase velocity matches the initial perpendicular speed of the beam ions ($\frac{\omega}{k} = u_0$), normalised as $\frac{u_0}{v_A}$, around $(\omega, k) \simeq (35, 600)$ in normalised units. This leads to a continuum like feature near the intersection, along with the harmonics excited along the $\frac{u_0}{v_A}$ line. A magnified image of the intersection region of figure 4 can be seen in figure A1 with the color scale rescaled to show it clearly. We explore this further using figure 7, which shows the MCI linear growth rates across the (ω, k) space for the same parameters for figure 4, with the fast ions initialised as a ring-beam distribution. The computationally enabled analytical linear calculations have been carried out using the code discussed in [52] which is constructed from generalised kinetic equations for the dielectric tensor elements. It is clear from comparisons of figures 4 and 7 that the outputs of our fully nonlinear PIC simulations carry an imprint of the linear MCI, particularly with respect to the following features. The harmonics are excited along the $\frac{u_0}{v_A}$ line and extend past the flattening of the fast Alfvén wave around the 35th harmonic. There is a broad range of waves excited close to the intersection of $\frac{u_0}{v_A}$ line with the fast Alfvén wave, i.e. around the 35th harmonic and dimensionless wavenumber 600. The splitting of harmonics observed in the simulations

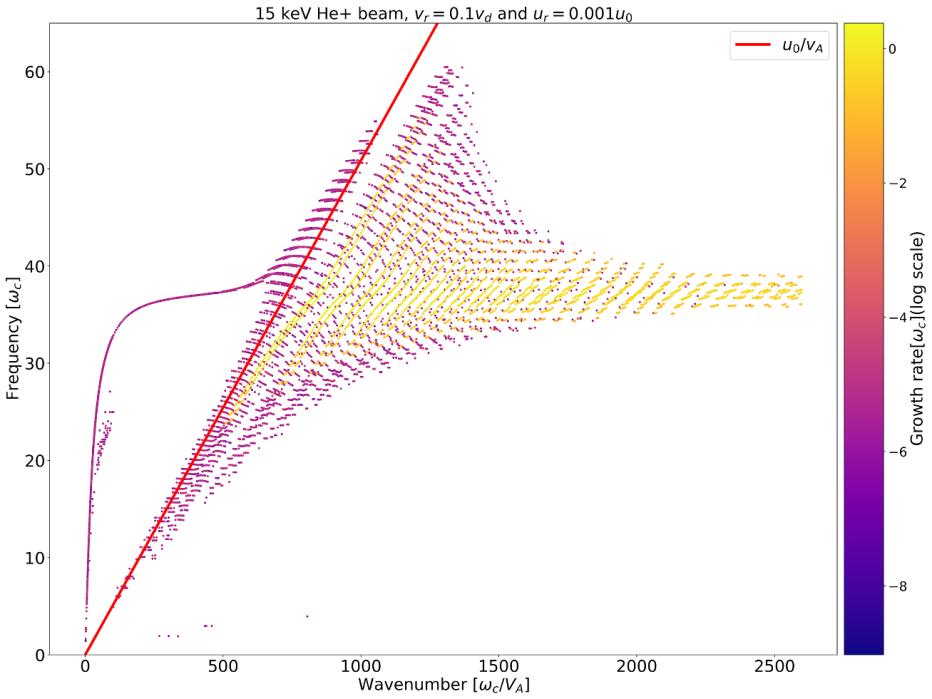

Figure 7. Linear growth rates of the MCI for the case of an He^+ LAPD plasma with 15 keV He^+ beam plotted in frequency wavenumber space. These results are obtained using the code of [52] for the first parameter set in table 1, with $n_e = 3 \times 10^{16}$ m^{-3}. The diagonal red line corresponds to $\frac{\omega}{k} = u_0$, normalised as $\frac{u_0}{v_A}$. It is evident that the linear MCI is concentrated at sequential ion cyclotron harmonics along the red line explaining the features observed in figure 4.

can also be seen in the linear calculations around this location. The formation of the $\frac{u_0}{v_A}$ line and the continuum like feature at its intersection with the fast Alfvén wave have previously been identified to be the case in figure 6 of [63] and figure 2 of [70]. Similar to the present study, all of these have sub-Alfvénic beams, meaning that the $\frac{u_0}{v_A}$ line is below the cold plasma dispersion, since $\omega \simeq kv_A$ at low frequencies.

3.3. Electrostatic versus electromagnetic aspects of ICE

As mentioned earlier in regard to figure 2, the minority ions primarily excite modes in the electrostatic field E_x in contrast to the electromagnetic field B_z. This comparison is important because it can help determine the appropriate diagnostics to measure ICE in experiments, as well as the other modes, such as lower hybrid, which are excited by the fast ions. It can also inform of mechanisms that nonlinearly excite linearly stable modes, thereby affecting the saturated power spectrum. In this section, we vary the energy of the beam ions from 15 keV to 150 keV while keeping other parameters in the H^+ beam column in table 1 the same to quantify its effect on the fields excited and the mechanism of energy transfer. Figure 8 shows how the ratio of the mean energy in the fluctuating part of B_z to that in E_x in our simulations varies with the parameter $\frac{v_\perp}{v_A}$. The dependence is almost linear, and the transition from predominantly electrostatic to electromagnetic is found close to $\frac{v_\perp}{v_A} \approx 0.4$. The time evolution of the particle and field energies which underpin figure 8, for 15 keV($\frac{v_\perp}{v_A} = 0.32$), 80 keV($\frac{v_\perp}{v_A} = 0.74$) and 150 keV($\frac{v_\perp}{v_A} = 1.013$) H^+ beam cases, can be seen in figure A2 in appendix. The rapid energy transfer shown in the three time traces of figure A2 is the MCI in action, through its linear and nonlinear phases. Corresponding plots of time evolution of the MCI in other, broadly similar contexts are given in figure 1 of [58], figure 9 of [42], figure 1 of [71] and figure 4 of [12]. The differences in the onset time of the initial linear phase of the MCI are related to the difference in energy or the 'distance' between the fast ion population and the thermal ions in the momentum space similar to other beam driven instabilities, for example see [72].

The dominant role of the electrostatic field component E_x, as compared to B_z, in the nonlinear interactions which further shape the LAPD ICE power spectrum can be inferred from comparing the bicoherence plots shown in figure 9 (left) and (right). Bicoherence [73, 74], defined and outlined for the present application in the appendix of [63], provides a robust quantitative measure of the strength of nonlinear coupling between two waves (k_1, k_2), and hence of nonlinear drive at a third wave, $k_1 \pm k_2$. Figure 9 shows nonlinear coupling primarily in E_x. Near the bottom of bicoherence plot of E_x in figure 9, for $k \lesssim 5$ we see the lower wavenumbers interacting with the structure around normalised wavenumbers (30–40, 0–5). These nonlinear couplings indicate an exchange of

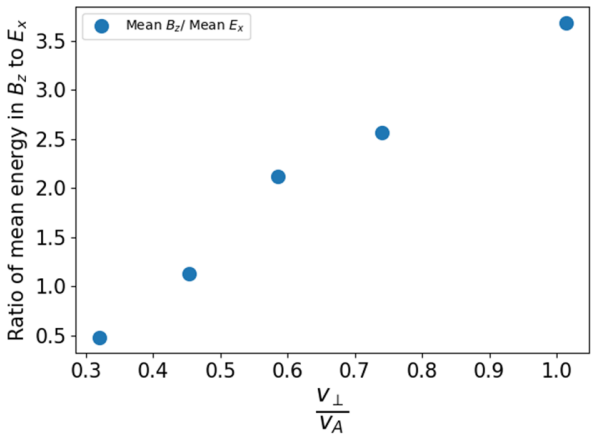

Figure 8. The ratio of average energy in the excited electromagnetic field component B_z to that in the electrostatic field component E_x in the PIC simulations of beam relaxation in LAPD plasmas, plotted versus initial perpendicular speed $v_\perp$ of the beam ions normalised to the Alfvén speed. We find approximately linear scaling with respect to the key parameter $\frac{v_\perp}{v_A}$. The transition from predominantly electrostatic to electromagnetic occurs around $\frac{v_\perp}{v_A} \approx 0.4$.

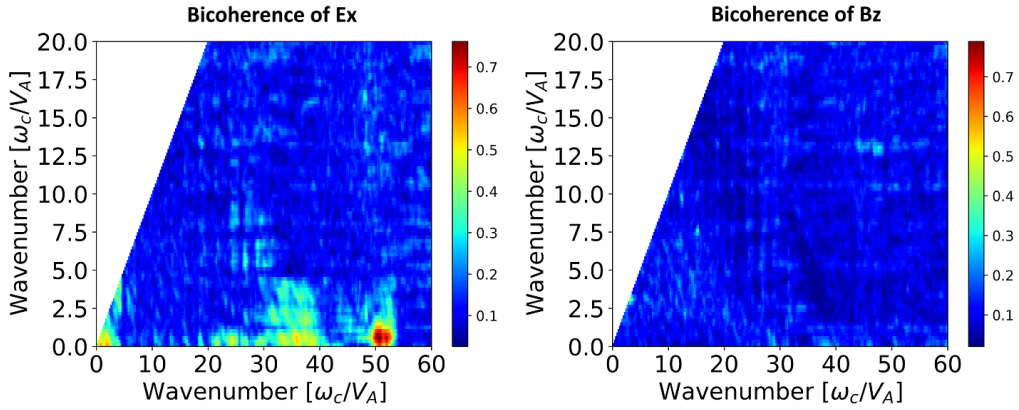

Figure 9. Bicoherence of the electric field E_x(left) and magnetic field B_z(right) for the He plasma with 15 keV H+ beam case. The key difference between the two bicoherences is the coupling visible at the bottom of E_x and absent from B_z. These nonlinear electrostatic interactions of the lower harmonics with the intermediate and high wavenumbers corresponding to the higher harmonics also influence the ICE spectra.

energy, possibly driving some of the modes which are linearly stable and, therefore, absent from figure 7.

4. Conclusions

The approach to simulating ICE adopted here, in relation to observations from the cylindrical LAPD plasma, is identical to that adopted for ICE observations from toroidal MCF plasmas in [11–13, 15, 23, 41–43, 45–47, 58]. This approach assumes slab geometry, as does the analytical linear theory of the MCI applied to ICE from MCF plasmas [9, 10, 50, 66, 75, 76], which of course predates the use of PIC codes exploiting high performance computation, as here. Slab geometry omits any physical effects that arise from toroidal magnetic field geometry. Its success in the MCF ICE context, in the sense of widespread qualitative and quantitative agreement between simulated and observed ICE power spectra, suggests that toroidal effects play a minor role, if any; and reinforces that ICE from toroidal MCF plasmas is a strongly spatially localised effect.

In the cylindrical LAPD facility, the plasma physics giving rise to the observed ICE spectrum is, by construction, exempt from toroidal effects. Hence, LAPD ICE is, in principle, better adapted than toroidal MCF ICE to our slab geometry simulation approach. It transpires, however, that the results presented here are exactly comparable to those from previous MCF-oriented simulations, in terms of:

(i) Congruence between simulated and observed ICE spectra. Counterparts to the combination here of figures 1, 5 and 6 include figure 1 of [45], figure 6 of [41], and figures 6 and 7 of [42].

(ii) Outputs quantifying the underlying physics. For example, counterparts to figure 2 include figure 2 of [45] for JET, figure 4 of [12] for KSTAR, and figure 9 of [42] for LHD. Counterpart FFTs to figures 3 and 4 include figure 5 of [12] and figure 8 of [42], and counterpart bispectral plots to figure 9 include figure 6 of [45] and figures 3 and 4 of [11].
(iii) Quantitative alignment with linear MCI theory where appropriate. Counterparts to figure 7 here include the middle panel of figure 1 of [45], and the combination of figures 2 and 3 of [46].

There is thus a mapping from the cylindrical LAPD ICE observations, via the PIC simulations presented here and elsewhere, to the toroidal MCF ICE observations. We conclude that the same underlying physics—namely, the MCI in its linear and saturated nonlinear phases—generates the observed signal. The LAPD spectra are instances of beam-driven MCI-type ICE in its sub-Alfvenic, predominantly electrostatic manifestation, which has precedents in MCF stretching back to TFTR [7, 8]. An interesting corollary, supported by the direct experimental ICE measurement which is interpreted and confirmed to be beam driven ICE in this paper, is that for many purposes ICE in toroidal MCF plasmas 'might as well' be occurring in a cylinder.

Acknowledgments

Calculations were performed using the Sulis Tier 2 HPC platform hosted by the Scientific Computing Research Technology Platform at the University of Warwick. Sulis is funded by EPSRC Grant EP/T022108/1 and the HPC Midlands+ consortium. S C C acknowledges support via the Johannes Geiss Fellowship of the ISSI, and AFOSR Grant FA8655-22-1-7056. The experiment was performed on the Large Plasma Device at the Basic Plasma Science Facility of UCLA, which is a DOE Office of Science, FES collaborative user facility funded by DOE (Award # DE-FC02-07ER54918) and the National Science Foundation (Award # NSF-PHY 1036140).

Appendix

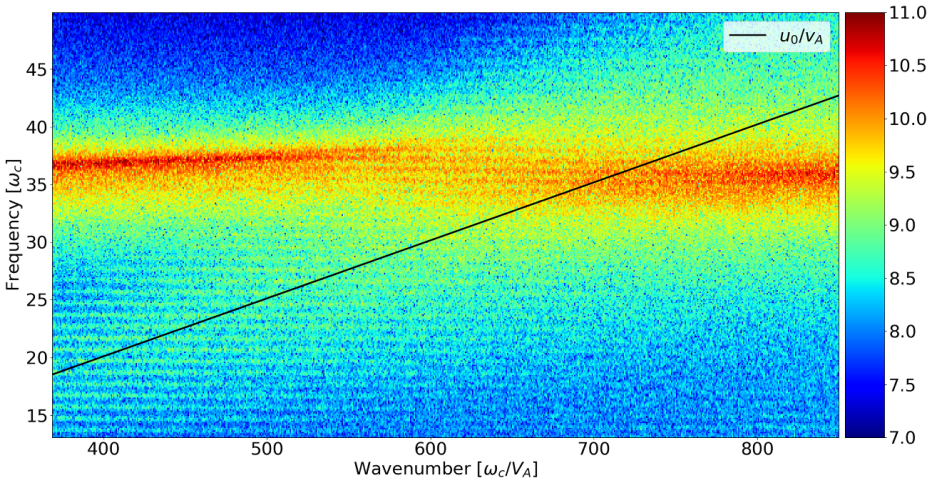

Figure A1. Magnified section of figure 4 showing the splitting and continuum like feature near the intersection of the dispersion of the fast Alfven wave and the line corresponding to where the phase velocity matches the initial perpendicular speed of the beam ions: $\frac{\omega}{k} = u_0$. The logarithmic (base ten) colour scale quantifies the relative distribution of energy across frequency-wavenumber space and has been rescaled compared to figure 4 to make this region clearer. Frequency is normalised to the singly ionised Helium cyclotron frequency $\omega_{c\mathrm{He}^+}$ and wavenumber to the ratio of $\omega_{c\mathrm{He}^+}$ to Alfvén velocity v_A.

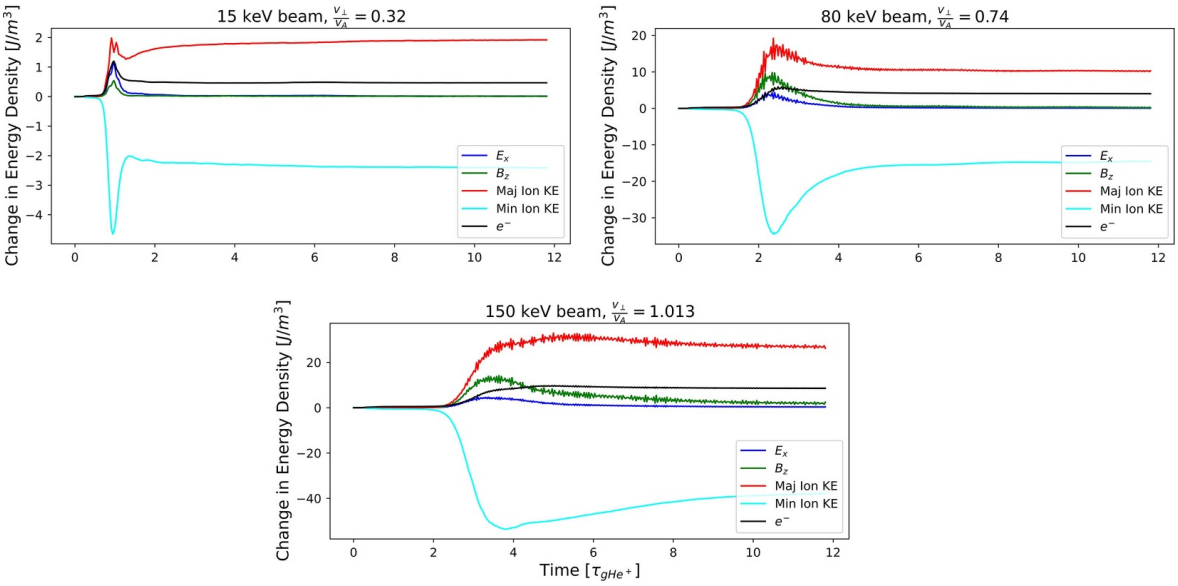

Figure A2. Time evolution of particle and field energy densities for three different beam energies for the He^+ plasma with H^+ beam. The key point to note is the relative amount of energy channelled to the electric and magnetic fields. The energy in the electrostatic component E_x dominates for 15 keV while the electromagnetic component B_z dominates in the other two cases. The 15 keV beam thus leads to an electrostatic ICE spectrum in the experimentally relevant case, whereas the conjectural 80 keV and 150 keV result in electromagnetic ICE.

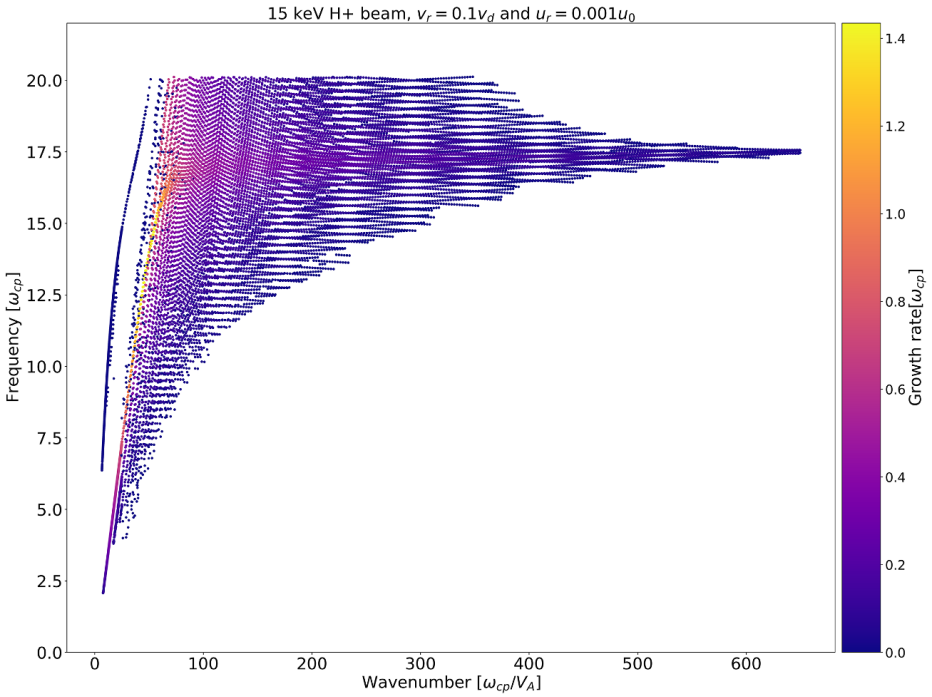

Figure A3. Linear growth rates of the MCI for the case of an He^+ LAPD plasma with 15 keV H^+ beam plotted in frequency wavenumber space. These results are obtained using the code of [52] for the second parameter set in table 1.

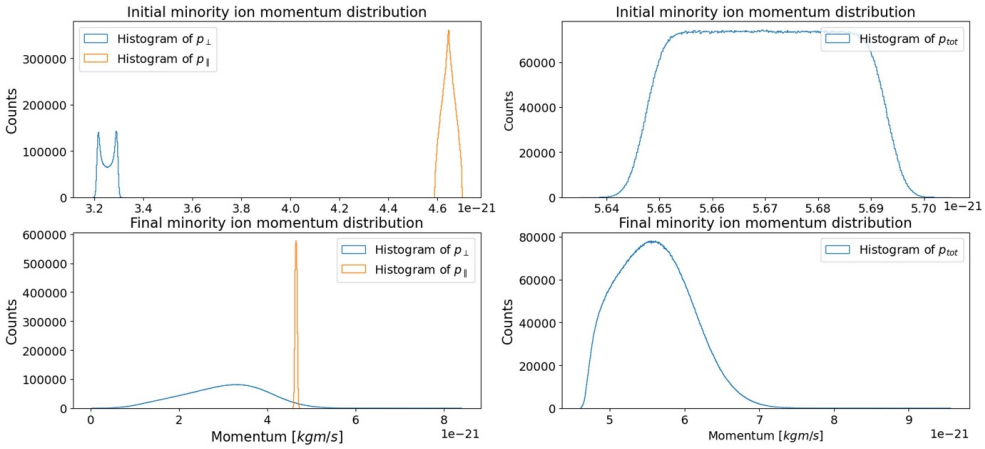

Figure A4. Initial and final He^+ beam distributions for the 15 keV He^+ beam case showing the relaxation of the beam ion population.

ORCID iDs

O. Samant https://orcid.org/0000-0002-2605-5363
R.O. Dendy https://orcid.org/0009-0002-0017-9103
S.C. Chapman https://orcid.org/0000-0003-0053-1584
S.K.P. Tripathi https://orcid.org/0000-0002-6500-2272
T. Carter https://orcid.org/0000-0002-5741-0495
B. Van Compernolle https://orcid.org/0000-0002-5853-6233
J.W.S. Cook https://orcid.org/0000-0002-1905-5218

References

[1] Gekelman W. *et al* 2016 The upgraded large plasma device, a machine for studying frontier basic plasma physics *Rev. Sci. Instrum.* **87** 025105
[2] Zhou S., Heidbrink W., Boehmer H., McWilliams R., Carter T., Vincena S., Tripathi S., Popovich P., Friedman B. and Jenko F. 2010 Turbulent transport of fast ions in the large plasma device *Phys. Plasmas* **17** 092103
[3] Cottrell G.A. and Dendy R.O. 1988 Superthermal radiation from fusion products in JET *Phys. Rev. Lett.* **60** 33
[4] Cottrell G.A., Bhatnagar V.P., Da Costa O., Dendy R.O., Jacquinot J., McClements K.G., McCune D.C., Nave M.F.F., Smeulders P. and Start D.F.H. 1993 Ion cyclotron emission measurements during JET deuterium-tritium experiments *Nucl. Fusion* **33** 1365
[5] Schild P., Cottrell G.A. and Dendy R.O. 1989 Sawtooth oscillations in ion cyclotron emission from JET *Nucl. Fusion* **29** 834
[6] McClements K.G., Hunt C., Dendy R.O. and Cottrell G.A. 1999 Ion cyclotron emission from JET D-T plasmas *Phys. Rev. Lett.* **82** 2099
[7] Cauffman S., Majeski R., McClements K.G. and Dendy R.O. 1995 Alfvénic behaviour of alpha particle driven ion cyclotron emission in TFTR *Nucl. Fusion* **35** 1597
[8] Cauffman S. and Majeski R. 1995 Ion cyclotron emission on the tokamak fusion test reactor *Rev. Sci. Instrum.* **66** 817–9
[9] Dendy R.O., McClements K.G., Lashmore-Davies C.N., Cottrell G.A., Majeski R. and Cauffman S. 1995 Ion cyclotron emission due to collective instability of fusion products and beam ions in TFTR and JET *Nucl. Fusion* **35** 1733
[10] Dendy R.O., McClements K.G., Lashmore-Davies C.N., Majeski R. and Cauffman S. 1994 A mechanism for beam-driven excitation of ion cyclotron harmonic waves in the tokamak fusion test reactor *Phys. Plasmas* **1** 3407–13
[11] Chapman B., Dendy R.O., Chapman S.C., McClements K.G., Yun G.S., Thatipamula S.G. and Kim M.H. 2018 Nonlinear wave interactions generate high-harmonic cyclotron emission from fusion-born protons during a KSTAR ELM crash *Nucl. Fusion* **58** 096027
[12] Chapman B., Dendy R.O., Chapman S.C., McClements K.G., Yun G.S., Thatipamula S.G. and Kim M.H. 2019 Interpretation of suprathermal emission at deuteron cyclotron harmonics from deuterium plasmas heated by neutral beam injection in the KSTAR tokamak *Nucl. Fusion* **59** 106021
[13] Chapman B., Dendy R.O., McClements K.G., Chapman S.C., Yun G.S., Thatipamula S.G. and Kim M.H. 2017 Sub-microsecond temporal evolution of edge density during edge localized modes in KSTAR tokamak plasmas inferred from ion cyclotron emission *Nucl. Fusion* **57** 124004
[14] Thome K.E., Pace D.C., Pinsker R.I., Van Zeeland M.A., Heidbrink W.W. and Austin M.E. 2019 Central ion cyclotron emission in the DIII-D tokamak *Nucl. Fusion* **59** 086011
[15] Zalzali A.I., Thome K.E., Dendy R.O., Chapman S.C., Chapman B., Cook J.W., Van Zeeland M.A., Crocker M.A. and DeGrandchamp G.H. 2021 Simulations of ion cyclotron emission from DIII-D tokamak plasmas *47th EPS Conf. on Plasma Physics* vol P4 p 1002
[16] DeGrandchamp G.H., Lestz J.B., Van Zeeland M.A., Du X.D., Heidbrink W.W., Thome K.E., Crocker N.A. and Pinsker R.I. 2022 Mode structure measurements of ion cyclotron emission and sub-cyclotron modes on DIII-D *Nucl. Fusion* **62** 106033
[17] Thome K.E., Pace D.C., Pinsker R.I., Meneghini O., Del Castillo C.A. and Zhu Y. 2018 Radio frequency measurements of energetic-particle-driven emission using the ion cyclotron emission diagnostic on the DIII-D tokamak *Rev. Sci. Instrum.* **89** 10I102
[18] Crocker N. *et al* 2022 Novel internal measurements of ion cyclotron frequency range fast-ion driven modes *Nucl. Fusion* **62** 026023
[19] DeGrandchamp G., Thome K., Heidbrink W., Holmes I. and Pinsker R. 2021 Upgrades to the ion cyclotron emission diagnostic on the DIII-D tokamak *Rev. Sci. Instrum.* **92** 033543
[20] Liu L. *et al* 2020 Explanation of core ion cyclotron emission from beam-ion heated plasmas in ASDEX-Upgrade by the magnetoacoustic cyclotron instability *Nucl. Fusion* **61** 026004
[21] Ochoukov R. *et al* 2018 Core plasma ion cyclotron emission driven by fusion-born ions *Nucl. Fusion* **59** 014001
[22] Ochoukov R. *et al* 2019 Interpretation of core ion cyclotron emission driven by sub-Alfvénic beam-injected ions via magnetoacoustic cyclotron instability *Nucl. Fusion* **59** 086032
[23] Chapman B., Dendy R., Chapman S., McClements K. and Ochoukov R. 2020 Origin of ion cyclotron emission at the proton cyclotron frequency from the core of deuterium plasmas in the ASDEX-Upgrade tokamak *Plasma Phys. Control. Fusion* **62** 095022
[24] Ochoukov R. *et al* 2018 Observations of core ion cyclotron emission on ASDEX-Upgrade tokamak *Rev. Sci. Instrum.* **89** 10J101
[25] Fredrickson E.D., Gorelenkov N.N., Bell R.E., Diallo A., LeBlanc B.P. and Podestà M. 2019 Emission in the ion cyclotron range of frequencies (ICE) on NSTX and NSTX-U *Phys. Plasmas* **26** 032111
[26] Fredrickson E., Gorelenkov N.N., Bell R.E., Diallo A., LeBlanc B.P., Lestz J. and Podestà M. (the NSTX team) 2021 Chirping ion cyclotron emission (ICE) on NSTX-U *Nucl. Fusion* **61** 086007
[27] Ichimura M., Higaki H., Kakimoto S., Yamaguchi Y., Nemoto K., Katano M., Ishikawa M., Moriyama S. and Suzuki T. 2008 Observation of spontaneously excited waves in the ion cyclotron frequency range on JT-60U *Nucl. Fusion* **48** 035012
[28] Sato S. *et al* 2010 Observation of ion cyclotron emission owing to DD fusion product H ions in JT-60U *Plasma Fusion Res.* **5** S2067–2067
[29] Sumida S., Shinohara K., Ikezoe R., Ichimura M., Sakamoto M., Hirata M. and Ide S. 2019 Characteristics of fast ^{3}He ion velocity distribution exciting ion cyclotron emission on JT-60U *Plasma Phys. Control. Fusion* **61** 025014
[30] Askinazi L.G., Belokurov A.A., Gin D.B., Kornev V.A., Lebedev S.V., Shevelev A.E., Tukachinsky A.S. and Zhubr N.A. 2018 Ion cyclotron emission in NBI-heated plasmas in the TUMAN-3M tokamak *Nucl. Fusion* **58** 082003
[31] Askinazi L. *et al* 2018 The spectrum of ion cyclotron emission from neutral beam injection heated plasma on the TUMAN-3M tokamak *Tech. Phys. Lett.* **44** 1020–3

[32] Askinazi L., Abdullina G., Belokurov A., Kornev V., Krikunov S., Lebedev S., Razumenko D., Tukachinsky A. and Zhubr N. 2021 Experimental determination of the dispersion relation of plasma radiation at frequencies of the ion cyclotron resonance and its harmonics in tokamak *Tech. Phys. Lett.* **47** 214–7

[33] Liu L.N. *et al* 2019 Ion cyclotron emission diagnostic system on the experimental advanced superconducting tokamak and first detection of energetic-particle-driven radiation *Rev. Sci. Instrum.* **90** 063504

[34] Liu L. *et al* 2020 Ion cyclotron emission driven by deuterium neutral beam injection and core fusion reaction ions in EAST *Nucl. Fusion* **60** 044002

[35] Liu L. *et al* 2023 Interpretation of ion cyclotron emission from sub-Alfvénic beam-injected ions heated plasmas soon after L-H mode transition in EAST *Plasma Phys. Control. Fusion* **66** 015007

[36] Liu L., Zhang X., Qin C., Zhao Y., Yuan S., Mao Y. and Wang J. 2019 High-frequency B-dot probes used to detect characteristics of ion cyclotron range of frequency waves in EAST *J. Plasma Phys.* **85** 905850214

[37] Liu L. *et al* 2023 Identification of core ion cyclotron instabilities on HL-2A tokamak *Nucl. Fusion* **63** 104004

[38] Tong R. *et al* 2022 Development of the ion cyclotron emission diagnostic on the HL-2A tokamak *J. Instrum.* **17** C01063

[39] Saito K. *et al* 2009 Measurement of ion cyclotron emissions by use of ICRF heating antennas in LHD *Fusion Eng. Des.* **84** 1676–9

[40] Saito K. *et al* 2013 Measurement of ion cyclotron emissions by using high-frequency magnetic probes in the LHD *Plasma Sci. Technol.* **15** 209

[41] Reman B.C.G., Dendy R.O., Akiyama T., Chapman S.C., Cook J.W.S., Igami H., Inagaki S., Saito K. and Yun G.S. 2019 Interpreting observations of ion cyclotron emission from large helical device plasmas with beam-injected ion populations *Nucl. Fusion* **59** 096013

[42] Reman B.C.G. *et al* 2021 Density dependence of ion cyclotron emission from deuterium plasmas in the large helical device *Nucl. Fusion* **61** 066023

[43] Reman B.C. *et al* 2022 First observation and interpretation of spontaneous collective radiation from fusion-born ions in a stellarator plasma *Plasma Phys. Control. Fusion* **64** 085008

[44] Saito K., Igami H., Toida M., Akiyama T., Kamio S. and Seki R. 2018 RF wave detection with high-frequency magnetic probes in LHD *Plasma Fusion Res.* **13** 3402043

[45] Carbajal L., Dendy R.O., Chapman S.C. and Cook J.W.S. 2014 Linear and nonlinear physics of the magnetoacoustic cyclotron instability of fusion-born ions in relation to ion cyclotron emission *Phys. Plasmas* **21** 012106

[46] Carbajal L., Dendy R., Chapman S.C. and Cook J.W.S. 2017 Quantifying fusion born ion populations in magnetically confined plasmas using ion cyclotron emission *Phys. Rev. Lett.* **118** 105001

[47] Carbajal L. and Calderón F. 2021 On the 2D dynamics of the magnetoacoustic cyclotron instability driven by fusion-born ions *Phys. Plasmas* **28** 014505

[48] Tripathi S., Van Compernolle B., Gekelman W., Pribyl P. and Heidbrink W. 2015 Excitation of shear Alfvén waves by a spiraling ion beam in a large magnetoplasma *Phys. Rev. E* **91** 013109

[49] Van Compernolle B., Tripathi S., Gekelman W., Pribyl P. and Colestock P. 2012 Ion beam generated modes in the lower hybrid frequency range in a laboratory magnetoplasma *39th EPS Conf. on Plasma Physics* (*Stockholm, Sweden, 2–6 July 2012*) vol P2 (available at: https://info.fusion.ciemat.es/OCS/epsicpp2012pap/pdf/P2.167.pdf) p 167

[50] Dendy R.O., Lashmore-Davies C.N., McClements K.G. and Cottrell G.A. 1994 The excitation of obliquely propagating fast Alfvén waves at fusion ion cyclotron harmonics *Phys. Plasmas* **1** 1918–28

[51] Belikov V. and Kolesnichenko Y.I. 1975 Magnetoacoustic cyclotron instability in a thermonuclear plasma *Sov. Phys.-Tech. Phys.* **20** 1146–51 (Engl. transl.)

[52] Cook J.W.S. 2022 Doublet splitting of fusion alpha particle driven ion cyclotron emission *Plasma Phys. Control. Fusion* **64** 115002

[53] Birdsall C. and Langdon A. 1991 *Plasma Physics via Computer Simulation* (IOP Publishing) vol 32

[54] Hockney R.W. and Eastwood J.W. 2021 *Computer Simulation Using Particles* (CRC Press)

[55] Arber T.D. *et al* 2015 Contemporary particle-in-cell approach to laser-plasma modelling *Plasma Phys. Control. Fusion* **57** 113001

[56] Chapman B., Dendy R.O., Chapman S.C., Holland L.A., Irvine S.W.A. and Reman B.C.G. 2020 Comparing theory and simulation of ion cyclotron emission from energetic ion populations with spherical shell and ring-beam distributions in velocity-space *Plasma Phys. Control. Fusion* **62** 055003

[57] Cook J.W.S., Dendy R.O. and Chapman S.C. 2013 Particle-in-cell simulations of the magnetoacoustic cyclotron instability of fusion-born alpha-particles in tokamak plasmas *Plasma Phys. Control. Fusion* **55** 065003

[58] Slade-Harajda T., Chapman S. and Dendy R. 2024 The consequences of tritium mix for simulated ion cyclotron emission spectra from deuterium-tritium plasmas *Nucl. Fusion* **64** 126051

[59] Bhadra D., Chiu S., Buchenauer D. and Hwang D. 1986 Electromagnetic emission from a neutral-beam-injected plasma *Nucl. Fusion* **26** 201

[60] Goede A., Massmann P., Hopman H. and Kistemaker J. 1976 Ion Bernstein waves excited by an energetic ion beam in a plasma *Nucl. Fusion* **16** 85

[61] Chang R. and Porkolab M. 1976 Experimental observation of the harris-type ion beam cyclotron instability *Nucl. Fusion* **16** 142–4

[62] McClements K.G., Dendy R.O., Lashmore-Davies C.N., Cottrell G.A., Cauffman S. and Majeski R. 1996 Interpretation of ion cyclotron emission from sub-Alfvénic fusion products in the tokamak fusion test reactor *Phys. Plasmas* **3** 543–53

[63] Samant O., Dendy R.O., Chapman S.C., Moseev D. and Ochoukov R. 2024 Predicting ion cyclotron emission from neutral beam heated plasmas in Wendelstein7-X stellarator *Nucl. Fusion* **64** 056022

[64] Cook J.W.S., Chapman S.C. and Dendy R.O. 2010 Electron current drive by fusion-product-excited lower hybrid drift instability *Phys. Rev. Lett.* **105** 255003

[65] Cook J.W.S., Chapman S.C., Dendy R.O. and Brady C.S. 2011 Self-consistent kinetic simulations of lower hybrid drift instability resulting in electron current driven by fusion products in tokamak plasmas *Plasma Phys. Control. Fusion* **53** 065006

[66] Dendy R., Lashmore-Davies C. and Kam K. 1993 The magnetoacoustic cyclotron instability of an extended shell distribution of energetic ions *Phys. Fluids B* **5** 1937–44

[67] Courant R., Friedrichs K. and Lewy H. 1928 Über die partiellen differenzengleichungen der mathematischen physik *Math. Ann.* **100** 32–74

[68] Atomic Molecular Data Services (AMDIS), IAEA 2012 Helium average charge states by flychk calculations (available at: www-amdis.iaea.org/FLYCHK/ZBAR/zbar002.html)

[69] Fitzpatrick R. 2022 *Plasma Physics: An Introduction* (CRC Press)

[70] Toida M., Saito K., Igami H., Akiyama T., Kamio S. and Seki R. 2018 Simulation study of high-frequency magnetosonic waves excited by energetic ions in association with ion cyclotron emission *Plasma Fusion Res.* **13** 3403015

[71] Dendy R., Chapman-Oplopoiou B., Reman B. and Cook J. 2023 Mechanism for collective energy transfer from neutral beam-injected ions to fusion-born alpha particles on cyclotron timescales in a plasma *Phys. Rev. Lett.* **130** 105102

[72] Kang H.L., Yoon Y.D., Cho M.-H. and Yun G.S. 2024 Fast nonlinear scattering of runaway electron beams through resonant interactions with plasma waves *Nucl. Fusion* **64** 106025

[73] Kim Y.C. and Powers E.J. 1979 Digital bispectral analysis and its applications to nonlinear wave interactions *IEEE Trans. Plasma Sci.* **7** 120–31

[74] de Wit T.D. 2003 Spectral and statistical analysis of plasma turbulence: beyond linear techniques *Space Plasma Simul.* (Springer) 315–43

[75] Dendy R., Lashmore-Davies C.N. and Kam K. 1992 A possible excitation mechanism for observed superthermal ion cyclotron emission from tokamak plasmas *Phys. Fluids B* **4** 3996–4006

[76] Dendy R. and McClements K. 1993 Ion cyclotron wave emission at the quasi-perpendicular bow shock *J. Geophys. Res. Space Phys.* **98** 15531–9